Thermoresponsive molecular brushes with propylene oxide/ethylene oxide copolymer side chains in aqueous solution

Jia-Jhen Kang,[1] *Florian A. Jung,*[1] *Chia-Hsin Ko,*[1] *Kaltrina Shehu,*[1,$] *Lester C. Barnsley,*[2,&] *Fabian Kohler,*[3] *Hendrik Dietz,*[3] *Junpeng Zhao,*[4,5] *Stergios Pispas*[5] *and Christine M. Papadakis*[1,*]

[1]Fachgebiet Physik weicher Materie, Physik-Department, Technische Universität München, James-Franck-Straße 1, 85748 Garching, Germany

[2]Jülich Centre for Neutron Science JCNS at Heinz Maier-Leibnitz Zentrum, Forschungszentrum Jülich GmbH, Lichtenbergstraße 1, 85748 Garching, Germany

[3]Laboratory for Biomolecular Design, Physik-Department, Technische Universität München, Am Coulombwall 4a, 85748 Garching, Germany

[4]Hefei National Laboratory for Physical Sciences at Microscale, University of Science and Technology of China, Hefei 230026, Anhui, China

[5]Theoretical and Physical Chemistry Institute, National Hellenic Research Foundation, 48 Vassileos. Constantinou Ave., 11635 Athens, Greece

Current affiliations:

[$] Heinz-Maier-Leibnitz-Zentrum (MLZ), Technische Universität München, Lichtenbergstr. 1, 85748 Garching, Germany

[&] Australian Synchrotron, ANSTO, 800 Blackburn Road, Clayton 3168, Australia

KEYWORDS: thermoresponsive polymers, solution behavior, molecular brushes, dynamic light scattering, small-angle neutron scattering, electron microscopy

TABLE OF CONTENTS GRAPHIC

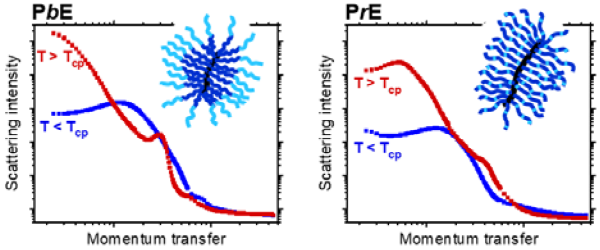

Abstract

The thermoresponsive behavior of two molecular brushes having poly(propylene oxide)-poly(ethylene oxide) copolymer side chains is investigated in aqueous solution, where the side chains have longer contour lengths than the backbone. The brushes differ in side chain architecture; they are either a diblock (P*b*E) or a random copolymer (P*r*E). For both types of brushes, an overall rod-like shape at room temperature is revealed by *cryo*-electron microscopy. A polymer-rich central part and a water-rich outer part is identified by small-angle neutron scattering (SANS). Upon heating up to the cloud point, the shell of P*b*E weakly dehydrates, while the one of P*r*E severely dehydrates along with a cylinder-to-disk transformation. Moreover, the aggregates formed above the cloud points feature significantly different inner structures: P*b*E aggregates are composed of strongly interpenetrating brushes, while P*r*E aggregates consist of loosely packed brushes. These differences indicate the important role of side chain architecture for the thermal dehydration behavior and the associated structural changes.

Introduction

Molecular brushes are densely grafted polymers composed of a backbone and numerous polymeric side chains.[1-3] At the backbone, the distance between neighboring chains is much smaller than their unperturbed dimension, which leads to a stretched conformation of both the backbone and the side chains due to the steric repulsion. Because of their compact structure, molecular brushes exhibit physical properties that differ from their linear analogues. In this study, we address molecular brushes with side chains exhibiting lower critical solution temperature (LCST) behavior.[4]

Linear polymers having LCST behavior are soluble in water at low temperatures, and become insoluble (or less hydrophilic) as the temperature is increased. The driving force for the lowered solubility is the unfavorable positive entropic contribution from the H-bonding between water and polymer, which becomes dominant in the free energy of mixing at high temperatures. Thus, upon heating, water molecules are released as the polymer-polymer interaction becomes more favorable. When the temperature is above the cloud point, T_{cp}, the dehydration induces a coil-to-globule conformational transition of the polymer chain.[5, 6] When LCST-type polymers are grafted on a polymeric backbone, such dehydration of the molecular brushes upon heating has been also observed,[7] yet T_{cp} is reduced due to the steric constraints and the prominent polymer-polymer interactions.[7, 8]

The size and shape of molecular brushes depend strongly on the molecular architecture, namely the backbone length, the side chain length and the grafting density,[9-14] which also has an influence on their structural evolution with temperature. For instance, when the backbone is significantly longer than the (LCST) side chains, a gradual decrease in the overall size with increasing temperature was observed in molecular brushes having poly(*N*-isopropyl acrylamide) side chains, and at T_{cp}, a cylinder-to-globule transition was found.[15] When the backbone and the side chains are of similar dimension, it was found that only the brush with long side chains shows a shrinkage in size with increasing temperature, while merely no change in size is observed for brushes with shorter side chains.[16]

The temperature-dependent structural investigations described above address molecular brushes with homopolymer side chains. Choosing copolymers of LCST type as side chains offers the possibility to tune the thermoresponsive behavior of the brushes by varying the composition or the architecture of the side chains. The general principle that random copolymerization of monomers with different properties results in polymers exhibiting intermediate characteristics of the constituent components,[17] is also realized in molecular brushes with random copolymers.[18-20] On the other hand, when the side chains are diblock copolymers, the thermoresponsive behavior of the molecular brush features transitions of both constituent polymer blocks.[18]

The described investigations on the behavior of thermoresponsive molecular brushes mostly rely on turbidimetry and dynamic light scattering (DLS), allowing to determine T_{cp} and the hydrodynamic radius, respectively. A detailed characterization of the structural evolution of thermoresponsive molecular brushes, especially around T_{cp}, relating the dehydration of brushes having different side chain architectures to their overall conformation and their inner structure has, to the best of our knowledge, not been carried out.

Another aspect in the difference between linear LCST type polymers and the molecular brushes is the aggregation behavior upon heating above the cloud point. As the temperature is increased, linear LCST polymers gradually interpenetrate and finally form large homogeneous aggregates due to the increasing hydrophobicity. In contrast, LCST molecular brushes form aggregates by agglomerating, and they only interpenetrate at the outermost periphery (if the side chains are long enough to allow such mobility).

In the present work, two molecular brushes with copolymer side chains are investigated in aqueous solution, the side chains being composed of propylene oxide (PO) and ethylene oxide (EO).[21, 22] Both PPO and PEO are thermoresponsive polymers exhibiting LCST behavior. The cloud point of PPO is lower than 8 °C,[23] while the one of PEO is higher than 100 °C.[24, 25] The two molecular brushes feature side chains having different architectures, namely diblock (PPO-*b*-PEO) or random P(PO-*r*-EO) copolymers named P*b*E and P*r*E, respectively. The PO weight fraction is ~60 wt% in both brushes. For both, the side chain contour length is longer than that of the backbone (Table 1), allowing for better observation on the effects caused by the side chain architecture.

PPO and PEO, in the form of linear block copolymers, have been applied as drug delivery systems, because of their good biocompatibility and tunable LCST behavior.[26, 27] Such linear block copolymers form micelles in aqueous solution, featuring a hydrophobic PPO core and a hydrophilic PEO shell. Molecular brushes with PPO-*b*-PEO side chains may be potential candidates for drug carriers, when the hydrophobic PPO blocks are attached to the backbone and create a hydrophobic nanodomain for drug storage. Molecular brushes with P(PO-*r*-EO) side chains may serve the same purpose, while the hydrophobicity of the core nanodomain can be adjusted by changing the composition between PPO and PEO. This provides an opportunity to optimize the molecular brushes, for instance to afford a moderate hydrophobicity, which has proven advantageous before.[28, 29] Detailed structural investigations around the cloud point are key to understand the formation of hydrophobic nanodomains and the switching process during encapsulation and release of the drug. Our previous research addressed the behavior of these brushes in dilute solution[21, 22] and their crystallization behavior in the melt.[30] In dilute solution, the cloud points T_{cp} and the hydrodynamic radii below T_{cp} were determined using light scattering. Fluorescence spectroscopy with pyrene revealed that P*r*E is strongly hydrated at low temperature and dehydrates gradually upon heating. Moreover, hydrophobic PPO domains could be identified within P*b*E.

Here, we address aqueous solution of P*b*E and P*r*E at higher concentrations than in the previous studies[21, 22] to investigate not only the inner structure of the brushes, but also their interactions below T_{cp} and their aggregation behavior above. *Cryo*-electron microscopy (*cryo*-EM) is used to characterize the shape of the individual brushes at room temperature. Temperature-resolved dynamic light scattering (DLS) measurements on semi-dilute solutions reveals that the cloud points are significantly lower than the ones of PEO homopolymers and differ from each other. To elucidate the origin of this reduction, we use small-angle neutron scattering (SANS) and identify the underlying changes of the inner structures and the water content of the two types of brushes. Moreover, the size and inner structure of their aggregates above the cloud point are investigated and are related to their dehydration process below the cloud point.

Experimental Section

Materials

The molecular brushes were synthesized by the grafting-from method.[21, 22] The backbone is poly(*para*-hydroxylstyrene) (PHOS), and the side chains are copolymers of ethylene oxide (EO) and propylene oxide (PO). The synthesis of P*b*E and P*r*E is described in detail in refs. 23 and 24. Their characteristics are compiled in Table 1. The lengths of the fully stretched backbones and side chains are calculated as the product of the monomer length and the degrees of polymerization, considering the C-C bond and C-O bond lengths and angles.[31] For *cryo*-EM, the polymers were dissolved in deionized water at a concentration of 2.5 g L^{-1}. For both DLS and SANS measurements, the solvent was D_2O (99.95%, Deutero GmbH) and the concentration was 20 g L^{-1} (in one case 5 g L^{-1}). All solutions were shaken at room temperature for at least 2 days before the experiments.

Table 1. Characteristics of the molecular brushes under investigation[21, 22]

Sample	$M_{\mathrm{w,bk}}$(a) [kg mol^{-1}]	Đ(b)	$M_{\mathrm{w,all}}$(c) [kg mol^{-1}]	$M_{\mathrm{w,sc}}$(d) [kg mol^{-1}]	DP_{bk}(e)	DP_{sc}(f)	L_{bk}(g) [nm]	L_{sc}(h) [nm]	f_{PO}(i) [%]	side chain architecture
P*b*E	10.5	1.18	1135	13.0	88	253	22.2	91.2	59.2	PPO-*b*-PEO with PPO near the backbone
P*r*E	17	1.22	1166	8.2	143	157	36.0	56.6	59.2	P(PO-*r*-EO)

[a] Weight-average molar mass of the backbone from size-exclusion chromatography. [b] $M_{\mathrm{w}}/M_{\mathrm{n}}$ for the backbone, from size-exclusion chromatography. [c] Overall molar mass from static light scattering. [d] Molecular weight of the side chains calculated from $M_{w,\mathrm{bk}}$ and $M_{\mathrm{w,all}}$, assuming a grafting density of 100%. [e] Weight-average degree of polymerization of the backbone calculated from $M_{\mathrm{w,bk}}$. [f] Weight-average degree of polymerization of the side chains calculated from $M_{\mathrm{w,sc}}$. [g] Estimated weight-average length of the fully stretched backbone. [h] Estimated weight-average length of the fully stretched side chain. [i] Weight fraction of PO in the molecular brush determined by ^{1}H NMR.

Methods

Cryo-Electron Microscopy. The sample solutions having a concentration of 2.5 g L^{-1} were applied to C-Flat 1.2/1.3 4C (Protochips, Morrisville, USA) grids and plunge-frozen using a Vitrobot Mark V (FEI, now Thermo Scientific) at a temperature of 22 °C and a humidity of 100 %. No waiting time was applied, the blot time was 2 s, the blot force parameter -1 and the drain time 0 s. The data were acquired using a Titan Krios G2 electron microscope operated at 300 kV equipped with a Falcon 3EC direct detector, a Volta Phase Plate (FEI, now Thermo Scientific), and a Cs Corrector (CEOS GmbH) using the EPU software for automated data and TIA software for manual data collection (FEI, now Thermo Scientific). Micrograph movies comprising 9-20 frames were recorded in linear and in counting mode at a calibrated magnification of 120k at a corresponding magnified pixel size of 0.53 Å, at a total dose of ~100 e^{-} $Å^{-2}$ and at a few hundred nanometer defocus, using the phase plate for contrast enhancement. The image processing was performed in RELION 2.1 and 3.0,[32, 33] using MotionCor2[34] to align the image frames. The software Fiji was used for the image analysis.[35]

Dynamic Light Scattering (DLS). DLS measurements were carried out using a LS Spectrometer from LS Instruments (Fribourg, Switzerland), which is equipped with a goniometer and two avalanche photodiode detectors. The light source was a polarized HeNe laser (Thorlabs, Dachau, Germany) with a maximum power 21 mW and a wavelength $\lambda = 632.8$ nm. Sample solutions were loaded in cylindrical glass cuvettes with 5 mm outer diameter and 0.4 mm wall thickness. The cuvette was mounted in a decalin bath, which was temperature–controlled by means of a Julabo CF31 *Cryo*-Compact Circulator (JULABO, Seelbach, Germany). The scattered intensity was collected at a scattering angle $2\theta = 90°$ and was recorded for 30 s. The normalized autocorrelation function of the scattering intensity, $g_2(q,\tau)$, is a function of the momentum transfer $q = 4\pi n \sin(\theta)/\lambda$, with n being the refractive index of the solvent, and the delay time τ. $g_2(q,\tau)$ was analyzed by the REPES algorithm implemented in the Gendist software, yielding average hydrodynamic radii (R_h).[36, 37] The distribution functions of R_h, A(R_h), are plotted in the equal area representation, R_hA(R_h) vs. logR_h. DLS data of 20 g L^{-1} solutions in D_2O were collected from 25 °C to 60 °C for P*b*E and from 25 °C to 38 °C for P*r*E, i.e., from room temperature to the respective cloud point T_{cp} of the solutions. At each temperature, 20 measurements were performed, giving a standard deviation of R_h after data analysis. The thermal equilibration time was set to 10 min.

Small-Angle Neutron Scattering (SANS). SANS measurements were performed at the KWS-1 instrument at the Jülich Centre for Neutron Science (JCNS) at Heinz Maier-Leibnitz Zentrum (MLZ), Garching, Germany.[38, 39] The neutron wavelength was λ = 5 Å ($\Delta\lambda/\lambda$ = 10 %), and the sample-to-detector distances (SDD) were 1.5 m, 8.0 m and 20 m, giving a q-range of 0.02-4.5 nm^{-1}. The exposure times were 8 min, 15 min and 30 min respectively, for the 3 SDDs. The detector was a Li scintillator with an active area of 60 cm × 60 cm and a spatial resolution of 5.3 mm × 5.3 mm. The solution samples were loaded into quartz glass cuvettes (Hellma Analytics) with a 2 mm neutron path. The cuvettes were mounted in a thermostated (Peltier) sample holder. Poly(methyl methacrylate) was used to bring the data to absolute intensity values and to provide the detector sensitivity. After the scattering from the empty cuvette was subtracted, and intensity matrices were corrected for transmission, the scattering intensity of the sample solutions were azimuthally averaged. Data reduction was conducted with the software QtiKWS by JCNS. SANS data of 20 g L^{-1} solutions in D_2O were collected from 25 °C to 64 °C for P*b*E, and from 25 °C to 42 °C for P*r*E, i.e., from room temperature to temperatures well above the respective cloud point T_{cp} of the solutions. The thermal equilibration time was set to 3 min.

Modeling of SANS Data. The SANS data of P*b*E were analyzed as follows. Below T_{cp}, the following model was used:

$$I(q) = I_0 P_{cs}(q) {S_{HS}}^{br}(q) + I_{bkg} \qquad (1)$$

I_0 is a scaling factor, $P_{cs}(q)$ the core-shell ellipsoid form factor, $S_{HS}^{br}(q)$ the hard-sphere structure factor, and I_{bkg} the incoherent background.

From $P_{cs}(q)$,[40, 41] the polar radius, R_p, and the equatorial radius, R_e, of the core of the brushes were resolved, as well as the shell thicknesses along both axes, T_p and T_e. The scattering length densities (SLD) of the core, ρ_{core}, and the shell, ρ_{shell}, were left as free fitting parameters, while the SLD of the solvent D_2O was fixed at 6.33×10^{-6} Å^{-2} (calculated from its mass density 1.1 g/cm^3). From their values along with the SLD values of PPO and PEO of 0.34×10^{-6} Å^{-2} and 0.64×10^{-6} Å^{-2},[42] the D_2O content in the core and the shell was determined.

The hard-sphere structure factor $S_{HS}^{br}(q)$ was applied to model the spatial correlation between the molecular brushes, using the Percus-Yevick approximation.[43] From this contribution, the hard-sphere radius, R_{HS}^{br}, i.e., half the center-to-center distance between the brushes, and the hard-sphere volume fraction, η^{br}, i.e., the volume fraction of brushes which are correlated, were obtained.

At T_{cp} (60 °C), the scattering contribution from large aggregates was included. Therefore, the fitting model read:

$$I(q) = I_{agg}(q) + I_0 P_{cs}(q) {S_{HS}}^{br}(q) + I_{bkg} \qquad (2)$$

For $I_{agg}(q)$, the empirical Guinier-Porod model was used:[44]

$$\begin{aligned} I_{agg}(q) &= \frac{G}{q^s}\exp\left[\frac{-(q{R_g}^{agg})^2}{3-s}\right] \quad for\ q \le q_1 \\ I_{agg}(q) &= \frac{D}{q^d} \quad for\ q \ge q_1 \end{aligned} \qquad (3)$$

G and D are the scaling factors of the Guinier term and the Porod term, respectively, which need to satisfy the requirement that the intensities of the two terms are equal at $q = q_1$. q_1 is calculated to meet the requirement of a smooth continuous curve, which yields:

$$\begin{gathered} q_1 = \frac{1}{q^s}\exp\left[\frac{-(qR_g{}^{agg})^2}{3-s}\right] \\ D = G\exp\left[\frac{-(qR_g{}^{agg})^2}{3-s}\right]q_1{}^{(d-s)} \end{gathered} \tag{4}$$

The Guinier term contains the radius of gyration of the aggregates, R_g^{agg}, and the shape factor, s, revealing the shape of the aggregates. $s = 0$ is found for spheres, $s = 1$ for thin rods, and $s = 2$ for flat disks. The Porod term provides information on the surface of the aggregates: The Porod exponent, d, describes the surface roughness of the aggregates. For a smooth surface, $d = 4$, while $d > 4$ indicates a concentration gradient at the surface of the aggregate.[45, 46]

At 62 °C, the contribution from the interacting brushes within the aggregates, was introduced. The model was:

$$I(q) = I_{agg}(q) + I_0 P_{fz}(q) S_{HS}{}^{br'}(q) + I_0 P_{cs}(q) S_{HS}{}^{br}(q) + I_{bkg} \tag{5}$$

It describes thus the scattering of the aggregates, of correlated brushes within the aggregates and of correlated brushes which are molecularly dissolved. The brushes within the aggregates are modeled by the fuzzy sphere form factor, $P_{fz}(q)$. It describes a homogeneous sphere with a fuzzy surface:[47]

$$P_{fz}(q) = \left\{\frac{3[\sin(qR_{fz}) - qR_{fz}\cos(qR_{fz})]}{(qR_{fz})^3}\exp\left(-\frac{(fq)^2}{2}\right)\right\}^2 \tag{6}$$

The fuzzy-sphere radius, R_{fz}, is the radius where the SLD has dropped to half of the value of the core. The fuzziness, f, is the width of the smeared surface. The radial SLD profile of a fuzzy sphere starts to decrease at $R_{fz} - 2f$ and reaches zero at $R_{fz} + 2f$. The hard-sphere structure factor $S_{HS}^{br'}(q)$ was combined with $P_{fz}(q)$, in order to describe the spatial correlations between the brushes composing the aggregates. $S_{HS}^{br'}(q)$ gives $R_{HS}^{br'}$ as well as $\eta^{br'}$, which are half the average distance between the constituent brushes in the aggregate and the volume fraction of these correlated brushes, respectively.

At 64 °C, the contribution from molecularly dissolved brushes disappears, and the model became:

$$I(q) = I_{agg}(q) + I_0 P_{fz}(q) S_{HS}{}^{br'}(q) + I_{bkg} \tag{7}$$

For P*r*E, the following model was used: Below T_{cp}, the same model as for P*b*E was used (Eq 1), but with an additional term to describe the intensity due to concentration fluctuations, presumably in the shell of $P_{\mathrm{cs}}(q)$. The model was thus expressed as:

$$I(q) = I_0 P_{cs}(q) S_{HS}{}^{br}(q) + I_{fluct}(q) + I_{bkg} \tag{8}$$

For $I_{\mathrm{fluct}}(q)$, a modified Ornstein-Zernike term was used:[48, 49]

$$I_{fluct}(q) = \frac{I_{OZ}}{1+(q\xi)^m} \tag{9}$$

I_{OZ} is a scaling factor and ξ the correlation length of concentration fluctuations. The exponent, m, provides information about the solvent quality for the polymer. $m = 5/3$ is expected for swollen polymers in a good solvent, $m = 2$ corresponds to Gaussian polymers in a theta solvent, while $m = 3$ is obtained for collapsed polymer chains in a poor solvent.

At and above T_{cp} (38 °C), the following expression was used:

$$I(q) = I_{agg}(q) S_{HS}{}^{agg}(q) + I_0 P_{fz}(q) S_{HS}{}^{br'}(q) + I_{fluct}(q) + I_{bkg} \tag{10}$$

$S_{\mathrm{HS}}{}^{\mathrm{agg}}(q)$ is the hard-sphere structure factor, which was used to describe the spatial correlation between the P*r*E aggregates. It gives the hard-sphere radius between the aggregates, $R_{\mathrm{HS}}{}^{\mathrm{agg}}$, as well as the volume fraction of the correlated aggregates, η^{agg}.

The incoherent background I_{bkg} was limited to values in the range 0.071 ± 0.003 cm^{-1} and 0.073 ± 0.003 cm^{-1} for P*b*E and P*r*E, respectively. The software SasView 4.1.2 was used for SANS model fitting.[50] The smearing effects were taken into consideration during software fitting by using a Gaussian function with standard deviation Δq as a weight function.

Results and Discussion

In the following, we present results from *cryo*-EM, which provides real-space images of the brushes; dynamic light scattering (DLS) reveals the size and LCST behavior, and small-angle neutron scattering (SANS), which gives detailed information on the structural changes in dependence on temperature.

Real-space Images

Fig. 1 shows the *cryo*-EM images of P*b*E and P*r*E solutions at 2.5 g L^{-1} in H_2O. Considering that the brushes are randomly distributed in the solution, oriented in all directions, the images should be seen as 2D projections of the brushes. Due to the high local electron density in the central part of the brushes, the dark lines in the images can be assigned to the polymeric backbones, while the greyish corona regions are composed of the crowded side chains. The length of the dark lines ranges from 15.6 to 20.1 nm for P*b*E, and from 17.0 to 36.5 nm for P*r*E. (For details see Fig. S1 and Tables S1 and S2 in the Supporting Information.) These wide ranges are supposed to be a result of the 2D projection from a 3D volume, as well as of the backbone polydispersity (Table 1).

We compare these values with the lengths of the fully stretched backbones, as estimated from the monomer lengths (Table 1). For P*b*E and P*r*E, 22.2 nm and 36.0 nm are obtained, respectively, which are close to the maximum values of the measured length of the dark lines in the *cryo*-EM images, for the corresponding brush. This implies that the backbones are stretched rather than having a Gaussian chain conformation, as observed previously.[13] Thus, the overall shape of the brushes in solution is expected to be elongated.

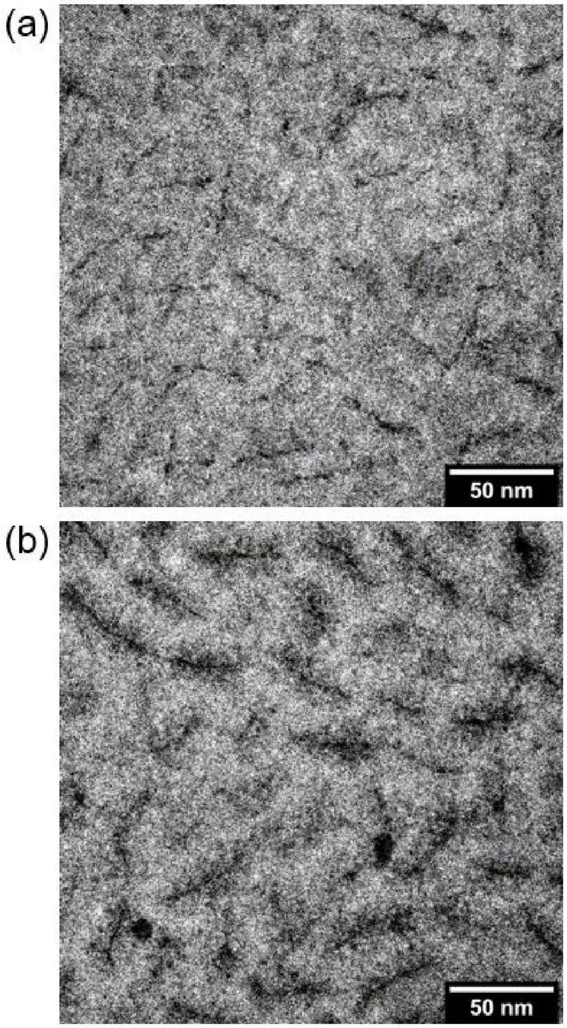

Figure 1. *Cryo*-EM images of (a) P*b*E and (b) P*r*E solutions at 2.5 g L^{-1} in H_2O.

Behavior Below T_{cp}

The behavior of the molecular brushes in aqueous solution below T_{cp} was characterized using dynamic light scattering (DLS). Measurements were performed on 20 g L^{-1} P*b*E and P*r*E solutions in D_2O, and temperature was increased, starting at 25 °C. D_2O was chosen for consistency with the neutron scattering experiments, which were carried out on the identical samples (see below). Representative autocorrelation functions and distribution functions are given in Fig. S2 in the Supporting Information. The dependence of the hydrodynamic radius, R_h, on temperature is given in Fig. 2. For both samples, R_h is around 16 nm at 25 °C, which is considered to be the hydrodynamic radius of an individual molecular brush. As the temperature is increased, R_h decreases by 2~3 nm, indicating the shrinkage of the side chains due to the increasing hydrophobicity. Upon further heating, R_h rises abruptly at the temperature where aggregates form, revealing the cloud point temperature T_{cp} of P*b*E and P*r*E solutions to be ~60 °C and ~38 °C, respectively. Above these temperatures, the high turbidity prohibits further DLS measurements. The significant difference in T_{cp} is due to the different distribution of the hydrophobic PO and the hydrophilic EO monomers. Presumably, in P*b*E, the hydrophobic PPO is located close to the backbone and is shielded from water by the hydrophilic PEO. In contrast, in P*r*E, the PO monomers are randomly distributed over the side chains, resulting in a much lower overall collapse temperature and thus lower T_{cp}. The R_h values for P*r*E are similar to the one observed previously at 1 g L^{-1}.[22] In contrast, the R_h values of P*b*E are ~2 nm smaller than the ones at 1 g L^{-1}.[21] The reason may be that the overall size of the molecular brush can be rather strongly affected by concentration, especially when the side chains are relatively long compared to the backbone (which is the case in P*b*E). As the side chains extend further away from the backbone, chain overlap is facilitated, which may alter the size.

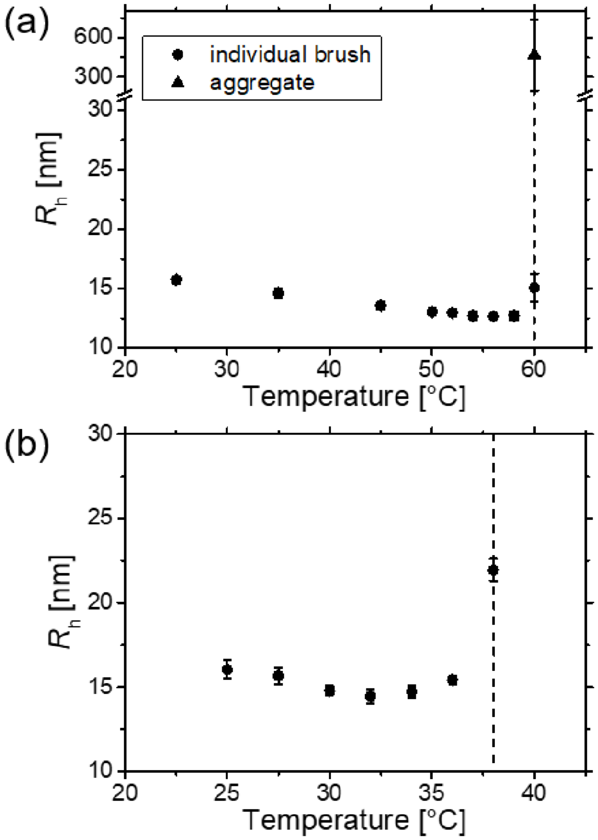

Figure 2. Hydrodynamic radii from DLS in dependence on temperature for 20 g L^{-1} solutions of (a) P*b*E and (b) P*r*E in D_2O. The vertical dashed lines indicate the resulting cloud point temperatures T_{cp}.

At the T_{cp} of the P*b*E solution, both individual molecular brushes and large aggregates are detected. On the contrary, no individual P*r*E molecular brushes are found at T_{cp}, and only aggregates are observed. We discuss this finding again below in the SANS analysis.

It was reported previously that the T_{cp} of a molecular brush with block copolymer side chain is close to the one of the block at the periphery.[18] However, our experimental result does not match this rule. T_{cp} of P*b*E solution is ~60 °C, i.e. much lower than the T_{cp} of the peripheral block, PEO, which is above 100 °C. It seems that T_{cp} is strongly reduced. To explain this finding, we consider the thermoresponsive behavior of self-assembled core-shell micelles formed by linear PEO-*b*-

PPO-*b*-PEO triblock copolymers in aqueous solution. Upon heating, the PEO-*b*-PPO-*b*-PEO chains rearrange with temperature, e.g., to alter the aggregation number in each micelle, until large aggregates are formed at T_{cp}.[51] As for a molecular brush with block copolymer side chains, P*b*E can be seen as a unimolecular core-shell particle, where the PEO-*b*-PPO diblock copolymers are tethered to the backbone, which makes it impossible to rearrange the chains upon a temperature change. Thus, the reduced T_{cp} for the molecular brush may be attributed to the effect of the grafting: Since a change in aggregation number is impossible, the phase transition takes place at a lower temperature. Besides the above, the hydrophobic PHOS backbone may also play a role in the reduction of T_{cp}.

Structural Analysis Around the Cloud Point

Overview. SANS measurements in a wide q range were conducted on 20 g L^{-1} solutions of both types of molecular brushes in D_2O to gain information about their structural evolution around their respective T_{cp}. From 25 to 58 °C, the scattering curves of P*b*E (Fig. 3a,c) show a broad maximum at ~0.1 nm^{-1} and an additional fringe at ~0.7 nm^{-1}. Upon heating towards 58 °C, both become less pronounced. Between 60 °C and 64 °C, the overall shape changes gradually. At 60 °C, strong scattering appears at low q, and steadily becomes more pronounced as the temperature is increased up to 64 °C. Meanwhile, the maximum at ~0.1 nm^{-1} becomes shallower and eventually vanishes at 64 °C. Another feature that shows up in this temperature range is the maximum at ~0.3 nm^{-1}, which emerges at 62 °C and grows more pronounced at 64 °C. Thus, significant changes are witnessed around T_{cp}, which we tentatively attribute to the collapse of the (outer) PEO blocks and the subsequent aggregation of the brushes, which, at 62 and 64 °C, seem to be strongly correlated within the aggregates. This is not the case at 60 °C, where we speculate that individual brushes coexist with loosely connected ones forming large aggregates, in consistency with the results from DLS at this temperature (Fig. 2a).

At higher temperatures (66 °C for P*b*E, 44 - 46 °C for P*r*E), SANS data do not show significant changes, and these are shown in Fig. S3 in the Supporting Information.

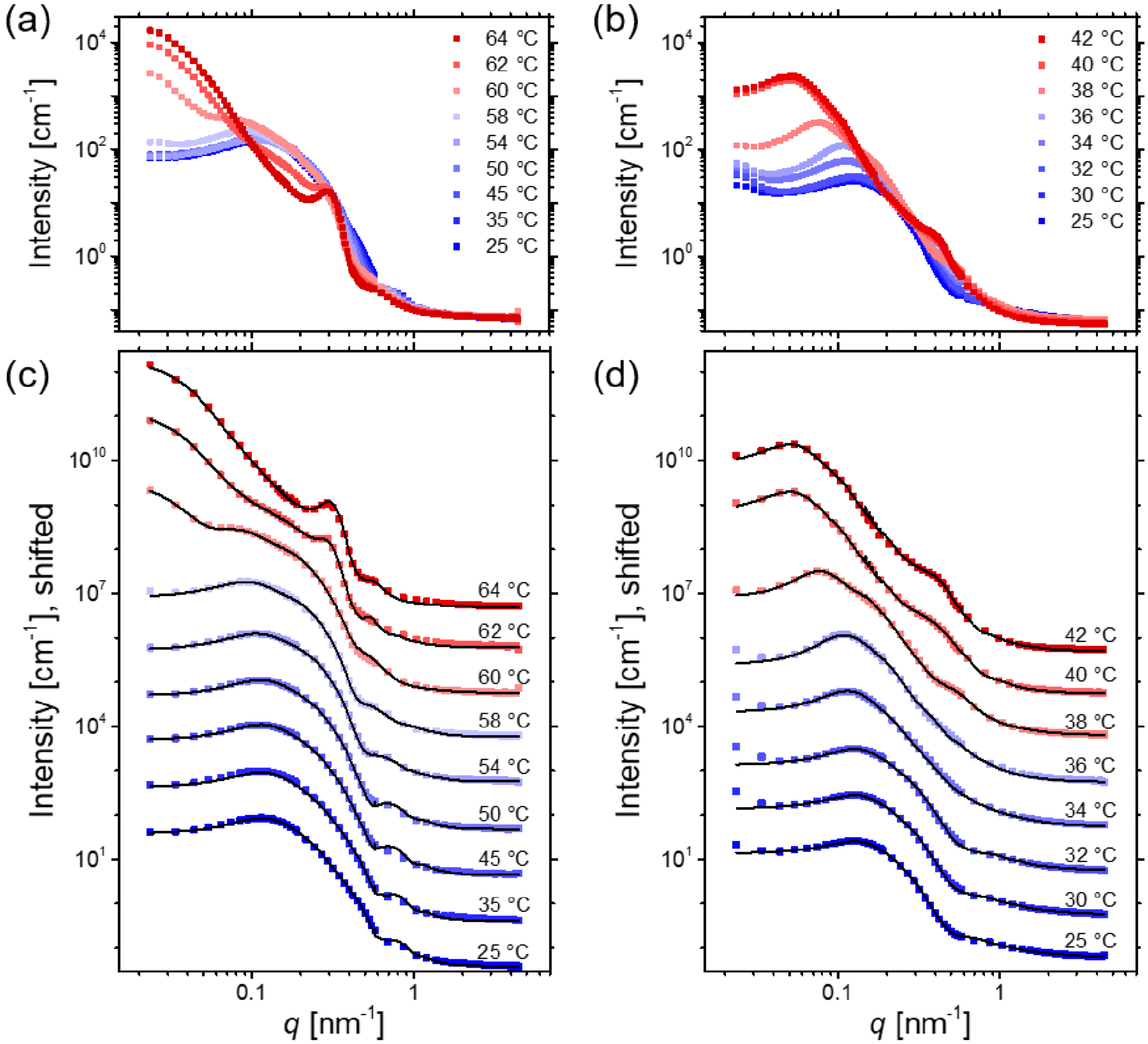

Figure 3. Representative SANS data of the 20 g L^{-1} solutions of P*b*E (a, c) and P*r*E (b, d) in D_2O (symbols) at the temperatures indicated in the graphs. The bluish and reddish colors indicate temperatures below and above the cloud point, respectively. In (c) and (d), the full lines are the model fits, see text. For better visibility, the data and the fits are shifted vertically by a factor of 10 with respect to each other in (c) and (d), and only every third data point is shown.

From 25 °C up to 36 °C, the features in the SANS data of P*r*E are similar to the ones of P*b*E in the same temperature range; however, they evolve in a different way: The maximum at 0.1 nm^{-1} becomes more pronounced upon heating towards 36 °C. Moreover, the shape of the decay between 0.1 and 1 nm^{-1} changes above 32 °C, and the maximum starts to move towards slightly lower q values (~0.1 nm^{-1}). At 38 °C, the maximum moves to substantially lower q values (~0.08 nm^{-1}), and its intensity increases drastically; moreover, fringes appear at ~0.2 and 0.7 nm^{-1}. At 40 and 42 °C, the position of the maximum is again decreased (~0.05 nm^{-1}), and its intensity is even higher; while the two fringes both move to lower q values. The strong scattering between 38 and 42 °C is attributed to large aggregates, which are correlated with each other. Thus, also in this sample, an intermediate state is encountered at T_{cp} (38 °C), where aggregates are gradually formed, grow and become correlated with each other.

Both solutions undergo distinct structural transitions upon an increase of temperature, which proceed in several steps. The temperatures, where aggregates appear, match the T_{cp} values determined by DLS rather well (60 °C for P*b*E and 38 °C for P*r*E). The structures of the two types of molecular brushes as well as their aggregates were analyzed by model fitting the SANS data using Eqs 1-10, as described in the Experimental Section. The fitted model curves are shown in Fig. 3c and d.

In both systems below T_{cp}, only dissolved brushes are present. For modeling their size, shape and inner structure below T_{cp}, the core-shell ellipsoid form factor is applied, assuming a polymer-rich core and a water-rich shell. This form factor is combined with the hard-sphere structure factor, which describes in the simplest possible way the spatial correlation between the brushes. While these two contributions are sufficient to obtain good fits for P*b*E (Fig. 4a, Eq. 1), an additional

Ornstein-Zernike term describing the decay of the P*r*E data at $q > 0.4\ \mathrm{nm}^{-1}$ is needed (Fig. 4b, Eq. 8), which we assign to concentration fluctuations in the shell.

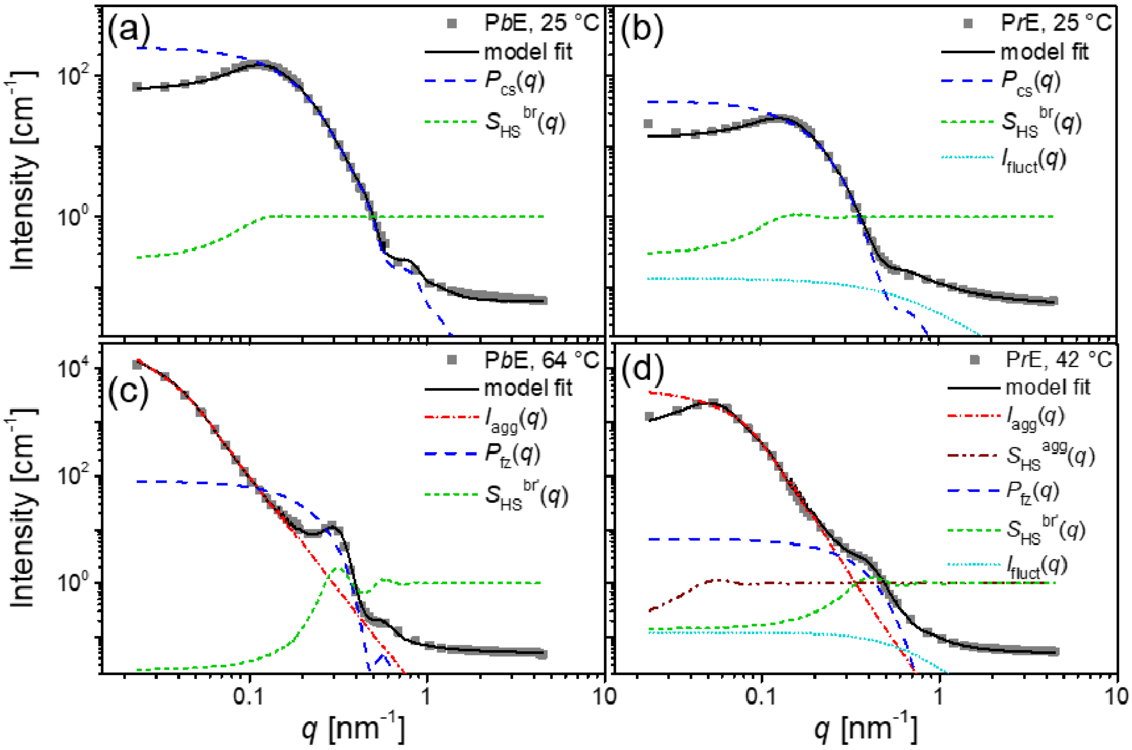

Figure 4. Model fits of the SANS data from 20 g L^{-1} P*b*E (a, c) and P*r*E (b, d) solutions in D_2O. Data below (a, b) and above (c, d) the respective T_{cp} (symbols), overall fits (black full lines) and contributions from each term in the fitting model (broken lines, see legend). The temperatures are given in the graphs. The contribution from the incoherent background is not shown.

For temperatures well above T_{cp} (Fig. 4c, d), the fuzzy sphere model is used, instead of the core-shell ellipsoid, to describe the molecular brushes that compose the aggregates, presumably because the side chains are collapsed. This form factor is again combined with the hard-sphere structure factor. In both solutions, the aggregate scattering is described by the Guinier-Porod form factor, and in the P*r*E solution, the correlation between aggregates is modeled by another hard-sphere structure factor. In addition, the model for the P*r*E solutions still includes the Ornstein-Zernike structure factor accounting for the scattering from concentration fluctuations. The SANS data well above the T_{cp} are thus model fitted by Eqs. 7 and 10 for P*b*E and P*r*E, respectively.

Besides, the data from the P*b*E solution at 60 and 62 °C seem to reflect coexistence of (i) dissolved brushes, which are of core-shell type and are correlated by the hard-sphere structure factor similar to the ones at lower temperatures, and (ii) molecular brushes which are of fuzzy sphere type and are located in the aggregates. Thus, P*b*E data at 60 and 62 °C are modeled by Eqs. 2 and 5, respectively. Using these models, excellent fits are obtained for both samples below, as well as above T_{cp}.

Two features may be noticed in the SANS data at the phase transition, both in P*b*E and P*r*E: a high intensity in the low-q region and fringes accompanied with correlation peaks at high q (0.3-0.4 nm^{-1}). For P*b*E, the two features appear in sequence as the temperature is increased; while for P*r*E, the two features both show up at $T_{\mathrm{cp}} = 38$ °C.

In the following, the structural parameters resulting from the different contributions to the model are discussed in dependence on temperature. Beginning with P*b*E and continuing with P*r*E, we address first the effect of the dehydration process below T_{cp} on the structure of the molecular brushes and describe afterwards the morphology and correlation of the aggregates. The differences of the dehydration process in P*b*E and P*r*E give information about the effect of the side chain architecture (block vs. random copolymer). The most important parameters are discussed below; full sets of structural parameters are compiled in Tables S3-S6 in the Supporting Information.

Structural Changes in the PbE Solution. Below T_{cp}, the molecular brush P*b*E is modeled as a core-shell particle. At 25 °C (i.e., far below T_{cp}), the polar and the equatorial radius of the core have similar values (~7 nm, Fig. 5a), while the shell is significantly thicker in polar direction (~

17 nm) than in equatorial direction (~ 4 nm, Fig. 5b). Altogether, this results in an elongated shape of the molecular brush. The scattering length density (SLD) of the core is ~0.6 × 10^{-6}Å^{-2} (Fig. 5c), which is close to the value of PPO (SLD 0.34 × 10^{-6}Å^{-2}). Assuming that the core consists of PPO and D_2O only, a content of D_2O of ~3 vol% is estimated. Thus, the core is spherical and compact and mainly composed of the backbone and the hydrophobic PPO blocks, which are water-insoluble and collapsed. The shell SLD amounts to 5.47 × 10^{-6} Å^{-2} at 25 °C (Fig. 5d). Assuming that the shell consists of PEO (SLD 0.64 × 10^{-6} Å^{-2}) and D_2O gives a water content of 84.9 vol%, i.e., it is very rich in water at room temperature.

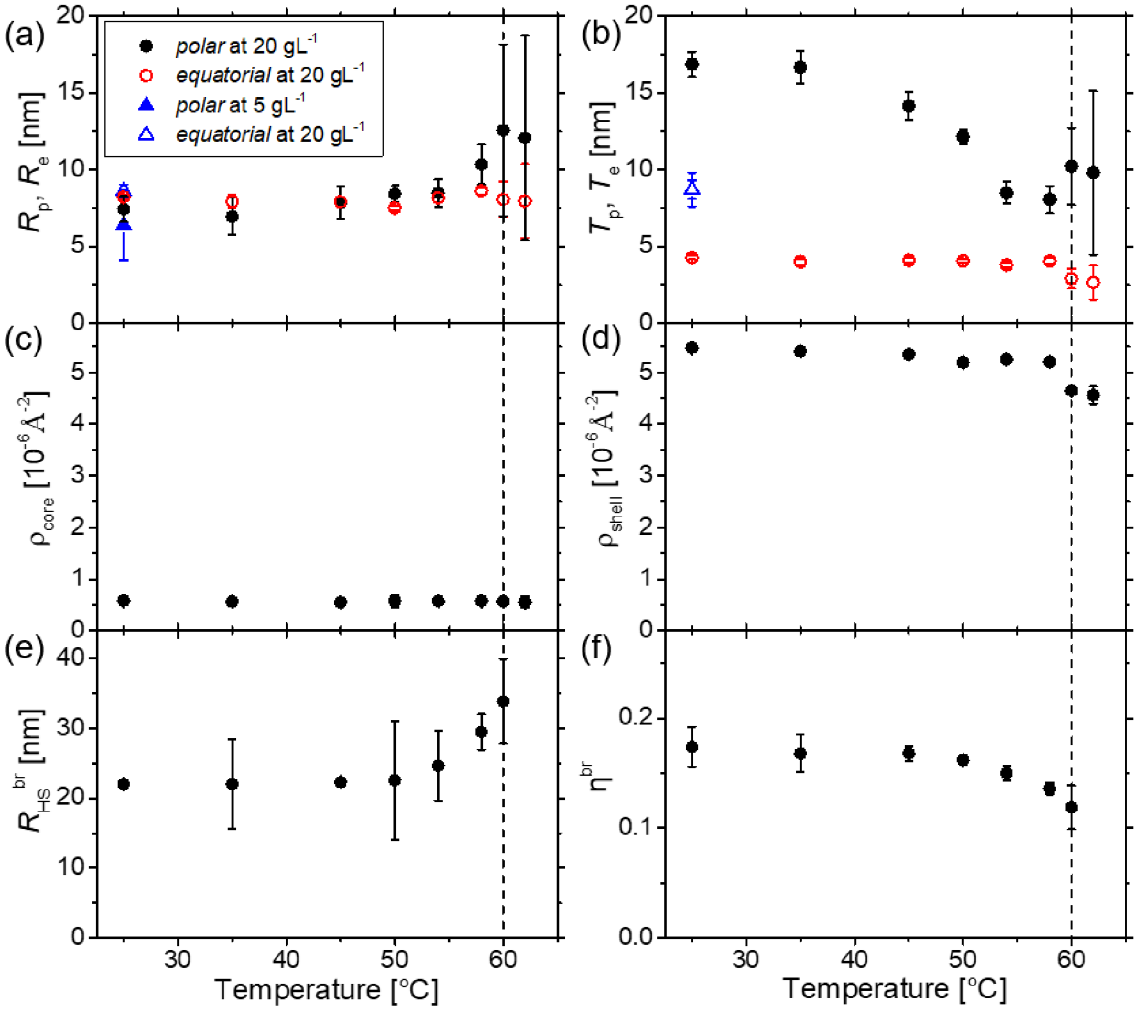

Figure 5. Structural parameters from model fitting to the SANS data of the 20 g L^{-1} solution of P*b*E in D_2O shown in Figure 4a in dependence on temperature from room temperature to around T_{cp}. (a) Core radii along polar and equatorial direction, R_p (closed black circles) and R_e (open red circles). (b) Shell thickness along polar and equatorial direction, T_p (closed black circles) and T_e (open red circles). Scattering length density in the core, ρ_{core} (c), and the shell, ρ_{shell} (d). (e) Hard-sphere radius R_{HS}^{br}. (f) Hard-sphere volume fraction η^{br}. The vertical dashed lines indicate T_{cp} from DLS. The blue triangles in (a) and (b) are parameters from a 5 g L^{-1} solution of P*b*E in D_2O (see Fig. S4 and Table S7 in the Supporting Information).

As for the shell, the inequality in the polar and equatorial shell thickness seems counterintuitive, since one would expect the side chains to stretch equally in all directions. In order to investigate whether this effect is due to close packing and mutual influence of the brushes at the concentration of 20 g L^{-1}, SANS data were also collected from a solution of significantly lower concentration, namely 5 g L^{-1} in D_2O (Fig. S4 in the Supporting Information). These data were analyzed in the same way as the ones at 20 g L^{-1} at 25 °C, resulting in an excellent fit. The resulting dimensions from the core-shell ellipsoid model are given in Fig. 5a and b. The analysis reveals that the core is also spherical with a similar size as in the 20 g L^{-1} solution (6.4 and 8.6 nm in polar and equatorial direction, Table S7 in the Supporting Information). However, the shell thickness is the same in all directions, namely 8.7 nm, which is between the polar and the equatorial value at 20 g L^{-1}. (The SLDs of the core and the shell are very similar to the ones at 20 g L^{-1}.)

Comparing the structure of the P*b*E molecular brush at 20 and at 5 g L^{-1}, it is seen that the size and the composition of the core, which is composed of the backbone, the PPO blocks and very little D_2O, is independent of concentration. In contrast, the shell, which contains the water-swollen PEO blocks, is sensitive to the concentration, which points to its flexibility. Whereas it has the same thickness all around the molecule in dilute solution, at higher concentration, the PEO blocks in the side chains arrange themselves such that the molecular brush assumes an elongated shape. The reason could be the mutual alignment of the molecular brushes along their polar direction, for the sake of reducing the interaction energy in equatorial direction, which is the explanation for elongated micelles formed by amphiphilic block copolymers.[52, 53] The elongated shape of P*b*E may thus be due to the relatively long side chains (the fully stretched side chain length is four times larger than the one of the backbone, Table 1). The thick, water-swollen PEO shell can change shape easily and adapt to the spatial limitation caused by the high concentration, leading to a rearrangement of the outer part of the side chains.

Looking again at the 20 g L^{-1}solution, upon heating towards T_{cp}, the core radii are unchanged up to ~45 °C. Above, the polar radius of the core increases and becomes slightly larger than the equatorial radius, namely R_p = 12 nm and R_e = 8 nm at 60 °C (Fig. 5a). Thus, the core shape transforms from spherical to slightly elongated. Meanwhile, the shell thickness in the polar direction continuously decreases as the temperature is increased (Fig. 5b). Up to ~45 °C, the decrease is weak (down to ~14 nm), but above, it is much stronger (down to ~8 nm at 58 °C). The shrinkage of the shell along the polar direction may be attributed to the dehydration of the PEO blocks and the resulting contraction, as the temperature is increased towards T_{cp}. The equatorial shell thickness is unchanged at ~4-5 nm in the entire temperature range up to T_{cp}. This value is slightly larger than the end-to-end distance of the PEO block, assuming Gaussian conformation, which is 3.9 nm (based on the monomer length of 0.359 nm, calculated based on the carbon-carbon bond length and the bonding angle).[31] Thus, the PEO blocks in the shell become increasingly dehydrated and rearrange, as T_{cp} is approached.

The scattering length density (SLD) of the core stays unchanged at ~0.6×10^{-6} Å^{-2} in the whole temperature range up to T_{cp} (Fig. 5c), i.e., the low content of D_2O of ~3 vol% is maintained. The shell SLD decreases weakly to 5.35×10^{-6} Å^{-2} at 45 °C and then more strongly to 4.64×10^{-6} Å^{-2} at 60 °C (Fig. 5d). This means, the water content decreases to 82.8 vol% at 45 °C and further to 70.3 vol% at 60 °C. Thus, the dehydration of the PEO-rich shell is very weak, even at 60 °C (i.e., the T_{cp} of the P*b*E solution).

The correlation between the P*b*E brushes is described by the structure factor $S_{HS}^{br}(q)$. For simplicity, the hard-sphere structure factor was chosen, which contains the hard-sphere radius R_{HS}^{br}, i.e., half the average distance between brushes in the solution, and the volume fraction of correlated brushes, η^{br}. At 25 °C, R_{HS}^{br} is ~22 nm and stays unchanged up to 50 °C (Fig. 5e). Above, it increases and reaches 32 nm at 60 °C. η^{br} also stays unchanged at 0.17 between 25 and 50 °C and slightly decreases to 0.11 at 60 °C (Fig. 5f). Both the rise of R_{HS}^{br} and the slight decrease of η^{br} are probably due to the overall shrinkage of the brushes above 45 °C, possibly also to the shape change towards a more spherical shape, as described above, resulting in an increased average distance and a weaker correlation.

The results reveal that the PEO blocks in P*b*E undergo a weak dehydration, as the temperature is increased from 45 °C towards T_{cp} (60 °C). Recalling the cloud points of PPO (8 °C) and PEO (>100 °C) homopolymers in aqueous solution, it can be concluded that, while the PPO blocks in the side chains are hydrophobic in the entire temperature range and form the dense core, the PEO blocks in the side chains gradually become more hydrophobic as the temperature is increased above ~45 °C, but still stays water-soluble up to 60 °C. Between 25 and 58 °C, the shell rearranges, the brushes become more spherical, and their correlation weakens, until aggregation finally sets in at 60 °C.

At 60 °C and above, a fraction of the brushes forms large aggregates, as evidenced by the abrupt increase of intensity at low q in the SANS data (Fig. 3a). Nevertheless, at 60 and 62 °C, a certain fraction is still dissolved as individual particles. They can be described as core-shell particles in the same way as at lower temperatures. The cores stay elongated (Fig. 5a), and the shell thickness in polar direction is larger than in equatorial direction (Fig. 5b). The SLDs remain unchanged (Fig. 5c and d). While the dissolved brushes are weakly correlated at 60 °C (Fig. 5e and f), they are not correlated any longer at 62 °C. At 64 °C, no contribution from dissolved brushes is observed in the SANS data, i.e., all brushes have become part of the aggregates. These observations imply that the phase transition of P*b*E starts with coexisting individual brushes and aggregates (60 °C); then, the contribution from the individual brushes decreases (62 °C) until only aggregates are present in the solution (64 °C).

We now turn to the characteristics of the aggregates and the brushes forming them. The aggregate scattering at low q values is described by the Guinier-Porod form factor (Fig. 4c), which gives the radius of gyration of the aggregates, R_g^{agg}, along with the shape factor s and the Porod exponent d. The contribution from the brushes within the aggregates, namely the correlation peak at q = 0.3 nm^{-1} as well as the fringe at 0.7 nm^{-1} are described by the fuzzy sphere form factor, $P_{fz}(q)$, combined with the hard-sphere structure factor, $S_{HS}^{br'}(q)$. These correlated fuzzy spheres are attributed to the dehydrated brushes that compose the aggregates. $P_{fz}(q)$ features the so-called fuzzy sphere radius R_{fz}, which is defined as the value where the SLD has decreased to half the value of the SLD of the core, and the width of the fuzzy surface, also called the fuzziness f. $S_{HS}^{br'}(q)$ gives half of the average distance between the correlated fuzzy spheres, $R_{HS}^{br'}$, and the hard-sphere volume fraction, $\eta^{br'}$. It is worth noting that $\eta^{br'}$ is the volume fraction occupied by the correlated brushes within an aggregate, rather than the normally considered volume fraction in the entire solution.

At 60 °C, R_g^{agg} is 73 nm, and it gradually decreases to 58 nm, as the temperature is increased to 66 °C (Fig. 6a). The continuous shrinkage of the aggregates may be related to the increasing hydrophobicity of the PEO block upon heating.[54] s is close to 0 and d around 4 (Fig. 6b,c), indicating the aggregates are spherical and have a smooth surface.

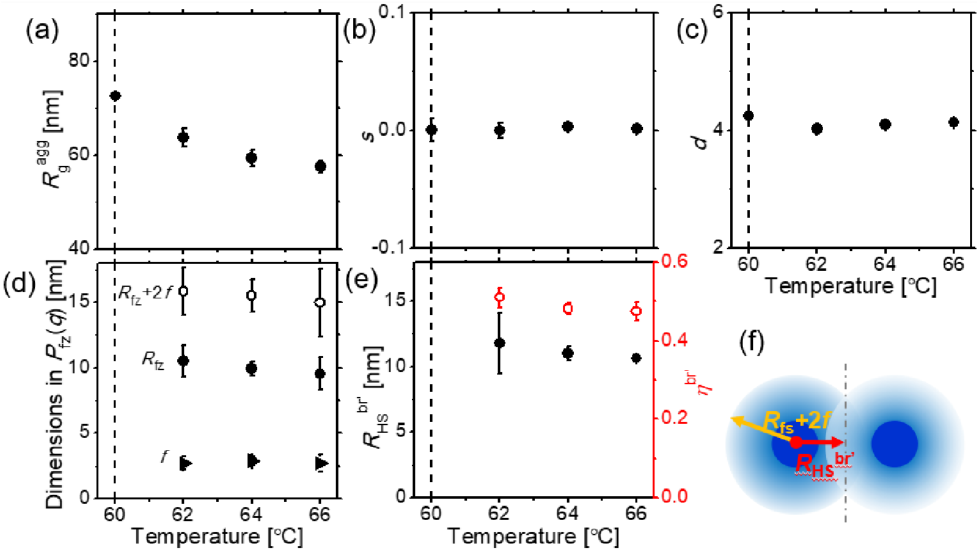

Figure 6. Structural parameters from model fitting to the SANS data of the 20 g L^{-1} solution of P*b*E in D_2O shown in Figure 4c in dependence on temperature at and above T_{cp}. (a) Radius of gyration of aggregates R_g^{agg}, (b) shape factor s, and (c) Porod exponent d. (d) Length scales from $P_{fz}(q)$: fuzzy-sphere radius R_{fz} (closed circles), fuzziness f (closed triangles) and R_{fz} + 2f (open circles). (e) Parameters from $S_{HS}^{br'}(q)$: hard-sphere radius $R_{HS}^{br'}$ (closed black circles, left scale) and volume fraction $\eta^{br'}$(open red circles, right scale). The vertical dashed lines indicate T_{cp} from DLS. (f) Schematic representation of the correlation between the brushes within the aggregates, comparing R_{fz} + 2f with $R_{HS}^{br'}$. The dash-dotted line indicates the center between two fuzzy spheres.

As for the dimensions of the brushes forming the aggregates, R_{fz} is 10 nm and f is 3 nm without temperature dependence (Fig. 6d). The SLD of the fuzzy sphere changes radially, starting from $R_{\mathrm{fz}} - 2f$ until $R_{\mathrm{fz}} + 2f$, where it reaches the solvent SLD value. Thus, $R_{\mathrm{fz}} + 2f$ is seen as the overall size of the fuzzy sphere. Comparing $R_{\mathrm{fz}} + 2f$ with $R_{\mathrm{HS}}^{\mathrm{br'}}$ can provide some insight into the packing of the brushes. While $R_{\mathrm{fz}} + 2f$ is around 16 nm, $R_{\mathrm{HS}}^{\mathrm{br'}}$ is only 11 nm (Fig. 6d,e), i.e., the side chains from adjacent brushes interpenetrate partly, as sketched in Fig. 6f. $\eta^{\mathrm{br'}}$ is found to be around 0.5, which is a rather high value. The overlapping fuzzy spheres and the high $\eta^{\mathrm{br'}}$ imply that the brushes within the aggregates are strongly connected.

Based on these results, a schematic view of the structural changes in dependence on temperature is derived, as shown in Fig. 7. At room temperature, P*b*E features a spherical core, presumably rich in PPO, and a water-swollen shell, presumably formed by PEO. The shell thickness is different along the polar and the equatorial direction, resulting in an elongated shape, in consistency with *cryo*-EM. This shape is attributed to the rather high polymer concentration. Upon heating, the shape changes towards a more spherical one. Below the cloud point, the dehydration of the shell is only weak, whereas above the cloud point, the brushes collapse and form large, spherical, smooth aggregates. Within the aggregates, the brushes interpenetrate.

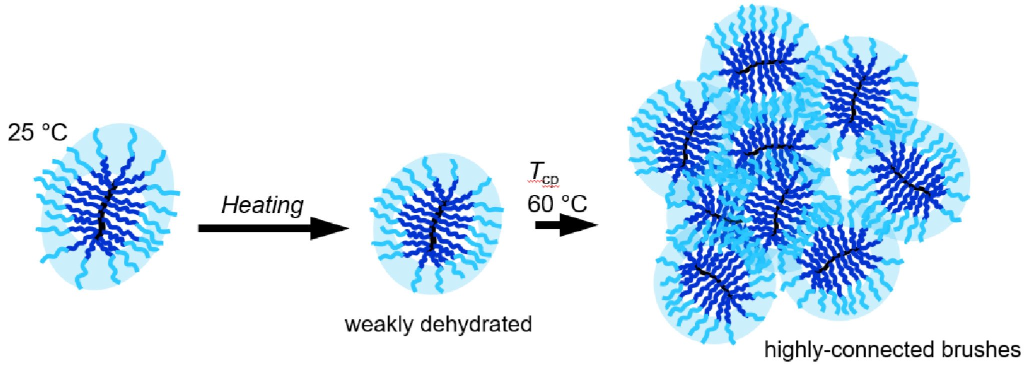

Figure 7. Schematic representation of the structural evolution of P*b*E in aqueous solution in dependence on temperature around the cloud point of 60 °C. The black arrows indicate the heating

process. The black, dark and light blue lines mark the polymeric backbone, the PO and the EO segments. A light blue shading indicates water.

Structural Changes in the PrE solution. We now turn to the structural changes in the 20 g L^{-1} P*r*E solution in D_2O below its cloud point T_{cp} = 38 °C. Again, the model of core-shell ellipsoids described the SANS data well in the q range 0.03-0.6 nm^{-1} (Fig. 4b), which indicates a polymer-rich inner part and a water-rich outer part of the brush. At 25 °C, the polar and equatorial core radii amount to 14 and 8 nm, and the shell thickness is 6 nm in both directions (Fig. 8a,b). Thus, P*r*E assumes an overall elongated shape like P*b*E, but in contrast to P*b*E at the same concentration, the core has an elongated shape, whereas the shell thickness is constant everywhere. Up to 32 °C, the polar core radius increases slightly to 16 nm, the equatorial core radius decreases slightly to 6 nm, while the shell thickness decreases by only ~1 nm in both directions. At 34 °C, the polar core radius is significantly lower, namely 6 nm, whereas the equatorial core radius has increased to 15 nm. Similar values are found at 36 °C. (Fits are shown in Fig. S5 in the Supporting Information.) Thus, above 32 °C, the core of the brushes assumes a disk-like conformation. The shell thickness along the polar axis decreases to ~1 nm, whereas it gradually decreases down to ~2.5 nm along the equatorial direction at 36 °C.

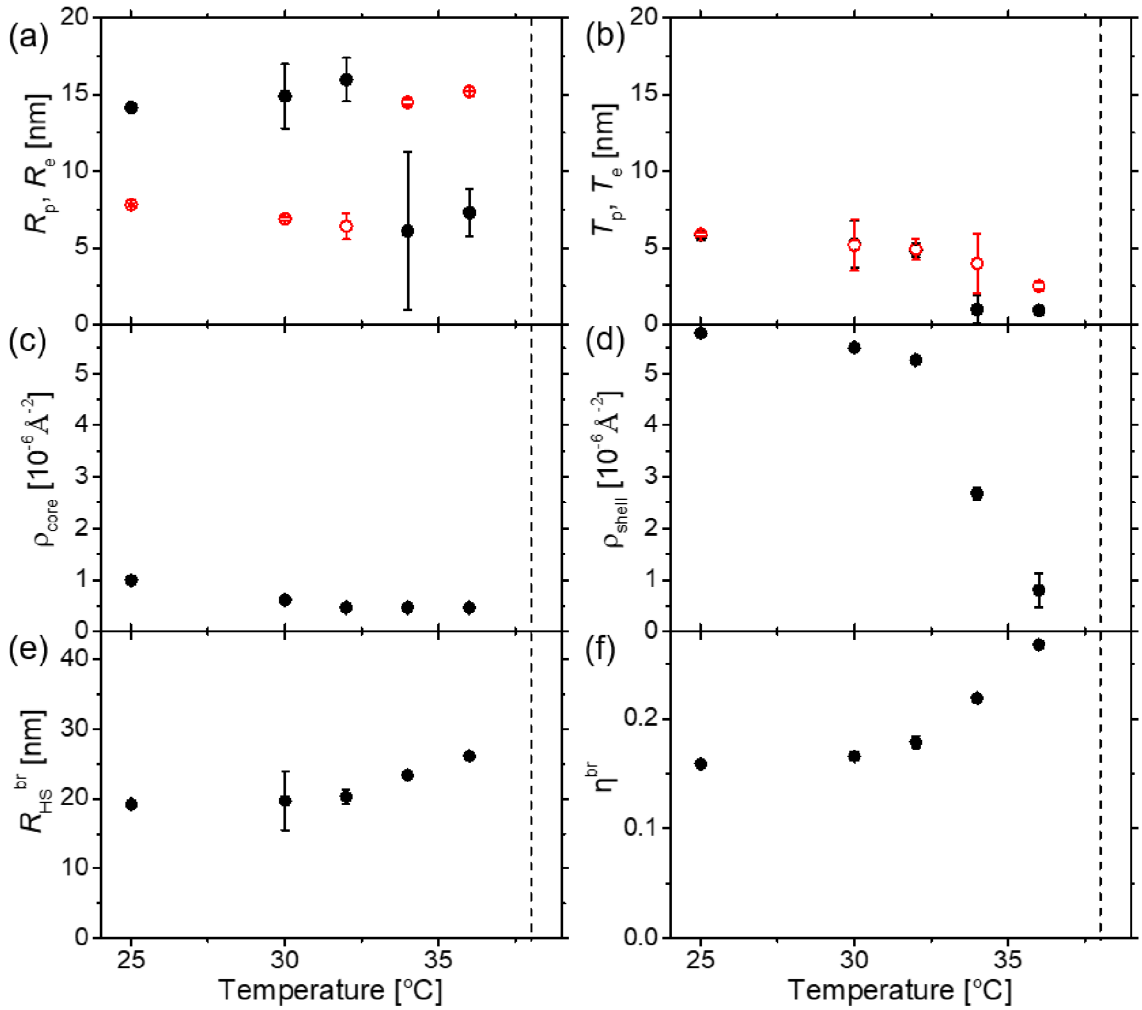

Figure 8. Structural parameters from model fitting to the SANS data of the 20 g L^{-1} solution of P*r*E in D_2O shown in Figure 4b in dependence on temperature below T_{cp}. (a) Core radii along polar and equatorial direction, R_p (closed black circles) and R_e (open red circles). (b) Shell thickness along polar and equatorial direction, T_p (closed black circles) and T_e (open red circles). The scattering length density in the core, ρ_{core} (c) and the shell, ρ_{shell} (d). (e) Hard-sphere radius R_{HS}^{br}. (f) Hard-sphere volume fraction η^{br}. The vertical dashed lines indicate T_{cp} from DLS.

These shape changes are accompanied by a dehydration of the core and the shell. The SLD of the core decreases from 25 °C to 32 °C and then stays unchanged up to 36 °C (Fig. 8c), while the SLD of the shell decreases first slightly up to 32 °C, then strongly up to 36 °C (Fig. 8d). Using the volume-weighted average SLD of PPO and PEO (0.43×10^{-6} Å^{-2}), these SLD changes correspond to a decrease of the water content in the core from 9.5 to 0.5 vol%, and, in the shell, a weak decrease from 90.7 vol% 25 °C to 81.9 vol% at 32 °C and then a strong decrease to 6.3 vol% at 36 °C. Thus, upon heating, water is repelled out of the P*r*E core and the shell, especially above 32 °C.

From the changes of the shape and of the water content of the core and the shell between 32 °C and T_{cp}, we conclude that the P*r*E brushes undergo a strong dehydration, leading to the collapse of the side chains. This might cause the backbone to coil up, resulting in the shape change from a rod-like to a disk-like particle.

The hard-sphere radius, related to the distance between the brushes, $R_{\mathrm{HS}}^{\mathrm{br}}$, is ~20 nm at 25-32 °C (Fig. 8e). Above, it increases to 26 nm at 36 °C. The volume fraction η^{br} is around 0.16 at 25 °C and increases to 0.27 at 36 °C (Fig. 8f). Thus, in the temperature range just below T_{cp}, both, the average distance between the brushes and the volume fraction of correlated brushes increase, which may seem counterintuitive. Comparing with the observations in P*b*E, where the volume fraction decreases upon heating towards T_{cp}, we suggest that the architecture of the side chains has an influence on the interaction between the brushes when approaching T_{cp}. In brushes with PPO-*b*-PEO side chains, the degree of dehydration of the PEO-rich shell is low, and the overall hydrophobicity changes only very little with temperature; moreover, no shape change is encountered. In contrast, the P(PO-*r*-EO) side chains in P*r*E release a large amount of water at 34 °C, thus, the shell becomes significantly more hydrophobic, which causes a stronger attractive interaction between the brushes. The simultaneous increase of the average distance between the brushes may be attributed to the drastic shape change of the P*r*E brushes, which affords a different arrangement between the neighboring brushes.

At 38 °C, the SANS curve shape is very different from the ones at lower temperatures (Fig. 3b,d). The maximum intensity is at a much lower q value, and fringes appear at both 0.2 and 0.7 nm^{-1}. The changes are attributed to the aggregate formation of the dehydrated brushes.

The data above 38 °C were fitted by a model similar to the one used for P*b*E above T_{cp}. It includes the Guinier-Porod form factor accounting for the size and shape of the aggregates, and the form factor of fuzzy spheres for the dehydrated brushes within the aggregates with the correlation between the latter being described by the hard-sphere structure factor, $S_{\mathrm{HS}}^{\mathrm{br'}}(q)$. Different from P*b*E, the P*r*E aggregates are correlated with each other, as is evident from the maximum at 0.5-0.7 nm^{-1} (Fig. 3b,d), and we model these interactions by another hard-sphere structure factor, $S_{\mathrm{HS}}^{\mathrm{agg}}(q)$.

The results reveal that, at 38 °C, the radius of gyration of the aggregates, $R_{\mathrm{g}}^{\mathrm{agg}}$ is only 14 nm (Fig. 9a). At higher temperatures, $R_{\mathrm{g}}^{\mathrm{agg}}$ becomes ~26 nm. The aggregates are spherical, since s ~0 (Fig. 9b). Applying the relation between the radius of gyration and the geometrical radius of a homogeneous spherical particle, we can estimate the radius of the aggregates, R, by $R = R_{\mathrm{g}}\,(5/3)^{1/2}$. R grows from 18 nm to 34 nm. Meanwhile, the hard-sphere radius of the aggregates, $R_{\mathrm{HS}}^{\mathrm{agg}}$, increases from ~39 to 57 nm (Fig. 9d) and is thus always about 20 nm higher than the radius of the aggregates, which means that the aggregates are well-separated from each other. The Porod exponent d is higher than 4 and close to 5, indicating a gradient SLD at the surface (Fig. 9c).

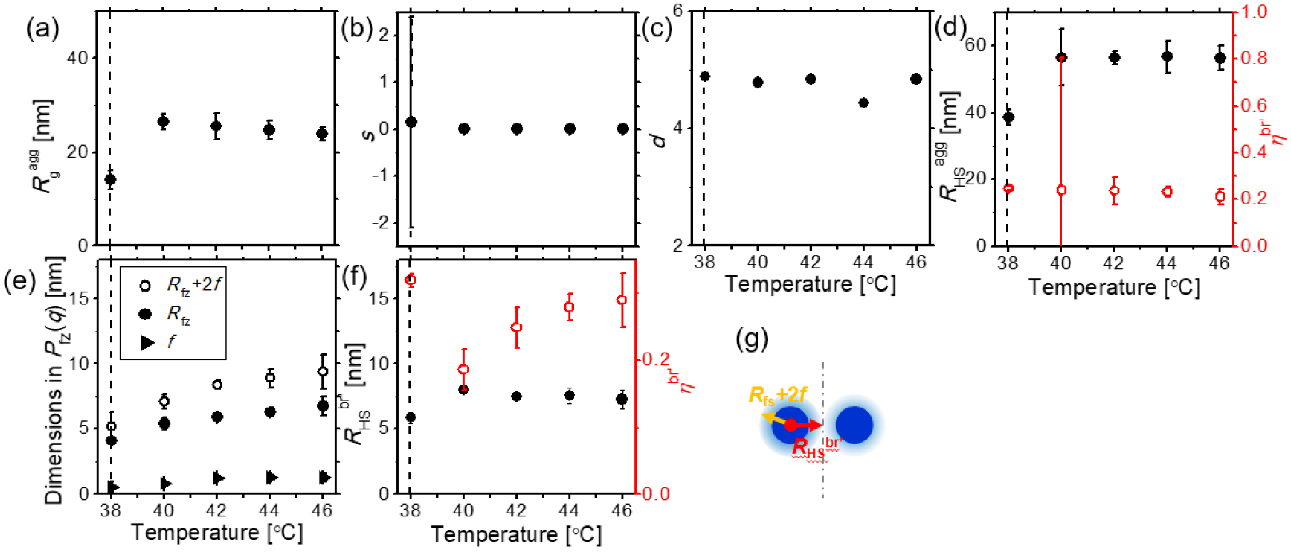

Figure 9. Structural parameters from model fitting to the SANS data of the 20 g L^{-1} solution of P*r*E in D_2O, as shown in Fig. 4d in dependence on temperature at and above T_{cp}. (a) Radius of gyration of the aggregates R_g^{agg}, (b) shape factor *s*, and (c) Porod exponent *d*. (d) Parameters from $S_{HS}^{agg}(q)$: hard-sphere radius R_{HS}^{agg} (closed black circles, left scale) and volume fraction η^{agg} (open red circles, right scale). (e) Length scales from $P_{fz}(q)$: fuzzy-sphere radius R_{fz} (closed circles), fuzziness *f* (closed triangles) and $R_{fz} + 2f$ (open circles). (f) Parameters from $S_{HS}^{br'}(q)$: hard-sphere radius $R_{HS}^{br'}$ (closed black circles, left scale) and volume fraction $\eta^{br'}$ (open red circles, right scale). The vertical dashed lines indicate T_{cp} from DLS. (g) Schematic representation of the correlation between the brushes within the aggregates, comparing $R_{fz} + 2f$ with $R_{HS}^{br'}$. The dash-dotted line indicates the center between two fuzzy spheres.

The data indicate a stepwise transition from 38 °C to 40 °C, above which the phase-separated solution reaches a stable state. In this temperature range, the aggregate size increases along with their average distance. Since no individual brushes are observed at 38 °C and above, aggregate growth may proceed via coalescence, which still seems possible up to 40 °C. Above, the growth stops, which we attribute to the strong dehydration of the brushes, rendering them rigid.

Regarding the brushes within the aggregates, their radius R_{fz} is 4 nm and the fuzziness f is 0.6 nm at 38 °C (Fig 9e), resulting in a $R_{\mathrm{fz}} + 2f$ value similar to $R_{\mathrm{HS}}^{\mathrm{br'}}$. Thus, the brushes are closely packed without interpenetrating each other (Fig, 9g), in contrast to the P*b*E brushes. Upon heating from 38 °C to 46 °C, $R_{\mathrm{fz}} + 2f$ values increase steadily, and become slightly higher than $R_{\mathrm{HS}}^{\mathrm{br'}}$. This might indicate that the brushes start to interpenetrate upon heating. This is supported by the volume fraction of correlated brushes, $\eta^{\mathrm{br'}}$, which shows a growth from 0.2 (40 °C) to 0.3 (46 °C) (Fig. 9f).

A modified Ornstein-Zernike structure factor was needed for P*r*E, both below and above T_{cp}, to describe the scattering at high q values, which is due to the concentration fluctuations of the polymer side chains (Fig. 4b, d). It features the correlation length, ξ, as well as the exponent, m, indicative of the polymer conformation.

The correlation length ξ fluctuates around 1.5 nm without any temperature dependence (Fig. 10a). From 25 °C to 36 °C, m increases from 1.8 to 2.8 (Fig. 10b), implying a decrease of the solvent quality, as expected. Above, it stays rather constant. The necessity of the modified Ornstein-Zernike term in the fitting model for P*r*E, which was not the case for P*b*E, indicates a higher degree of local inhomogeneity in the P*r*E solution, which might be due to the randomly distributed hydrophobic PO segments.

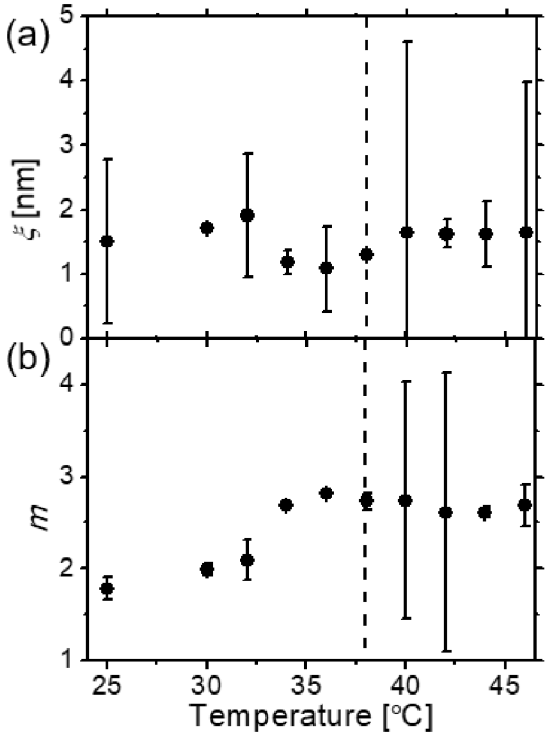

Figure 10. Parameters from the modified Ornstein-Zernike structure factor for the P*r*E solution: (a) correlation length ξ, (b) exponent m. The vertical dashed lines indicate T_{cp} from DLS.

Figure 11 shows a schematic view of the structural evolution of P*r*E. The brushes are elongated at room temperature and feature a swollen shell, in consistency with *cryo*-EM. A few degrees below the cloud point, the shell deswells strongly, and the brush changes shape to become a flat disk, presumably because the backbone folds. At the cloud point, the collapsed brushes gather to form aggregates, within which the brushes do not interpenetrate. Concentration fluctuations are still present above the cloud point.

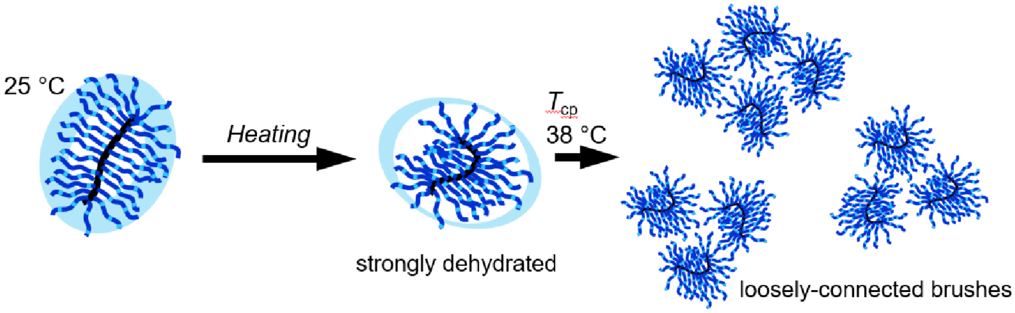

Figure 11. Schematic representation of the structural evolution of P*r*E in aqueous solution in dependence on temperature around the cloud point of 38 °C. The black arrows indicate the heating process. The black, dark and light blue lines mark the polymeric backbone, the PO and the EO segments. A light blue shading indicates water.

Comparison of the aggregation behavior of PbE and PrE. It is worth noticing that, above T_{cp}, R_g^{agg} is significantly larger for P*b*E and the surface is smoother than for P*r*E (Figs. 6a,b and Fig. 9a,b). Within the aggregates, the P*b*E brushes interpenetrate each other and are strongly correlated, which is not the case in P*r*E aggregates. Actually, the aggregates formed by P*r*E brushes may rather be considered as loose clusters.

The different aggregation behavior is related to the strong difference in the degree of dehydration of the molecular brushes at the cloud point, which concerns the mobility of the polymer chains.[55-57] However, the fuzzy sphere form factor used above T_{cp} does not contain information on the SLD; thus, the water content is a priori unknown. Here, we try to gain a rough idea about the degree of dehydration in the aggregates by comparing the size and shape of the individual dissolved brushes below T_{cp}, modeled as core-shell ellipsoids and the brushes within the aggregates above T_{cp}, modeled as fuzzy spheres. For P*b*E, the geometric mean radius, $R_{mean} = [(R_p + T_p) \times (R_e + T_e)^2]^{1/3}$, of the core-shell ellipsoid is ~14 nm at 58 °C, i.e., just below T_{cp}, which is similar to the overall radius of the fuzzy spheres at 62 °C ($R_{fz} + 2f \cong 16$ nm). Thus, it is reasonable to assume that the P*b*E brushes in the aggregates are as hydrated as the dissolved ones, i.e., their PEO shells contain 70 vol% D_2O. As for P*r*E, R_{mean} is ~14 nm at 36 °C, while the fuzzy spheres at 38 °C are much smaller ($R_{fz} + 2f$ ~6 nm). The severe shrinkage may imply that the P*r*E brushes in the aggregates are strongly dehydrated. Since the shell of P*b*E stays hydrated, the PEO blocks are mobile and can more easily connect and interpenetrate with those from other brushes. As a result, the P*b*E brushes are strongly correlated, and larger aggregates can form. As for P*r*E, the brushes are strongly dehydrated and are less mobile. This hampers the association with other brushes and thus slows down aggregate growth. As a result, small aggregates with a rather high surface roughness are encountered.

Another effect that influences the side chain mobility is the architecture of the molecular brushes. When the side chains are much longer than the backbone, it is easier for them to overlap with each other, and the side chains with higher mobility can interpenetrate with chains from neighboring brushes. On the other hand, when the side chains are short compared to the backbone, the brushes behave like bottle brushes that hardly overlap with adjacent brushes. The fact that P*b*E has longer side chains and a shorter backbone than P*r*E, is thus also considered as one of the reasons why the P*b*E aggregates are larger than the ones from P*r*E.

Conclusion

Cryo-electron microscopy, dynamic light scattering and small-angle neutron scattering are used to investigate the structure of molecular brushes in aqueous solutions. The molecular brushes under study feature thermoresponsive PPO-PEO diblock or random copolymer side chains. The linear PPO and PEO polymers exhibit vastly different cloud points.

As the temperature of the molecular brush solution is increased, starting from room temperature, the brushes with diblock copolymer side chains undergo a slight dehydration, and form aggregates with strong connections between the hydrated brushes. On the contrary, the molecular brushes with random copolymer side chains show severe dehydration upon heating, and the dehydrated brushes form aggregates by mere gathering without close connections.

The architecture of the side chains implies strong differences in the intra- and intermolecular interactions and the resulting brush shapes and inner structures in dependence on temperature, as well as in the size and inner structure of the aggregates. These features cannot be identified using turbidimetry, vibrational spectroscopy or light scattering. The wide *q*-range of small-angle neutron scattering reveals structures on a wide range of length scales. These findings may be related to the dehydration process of thermoresponsive molecular brushes with different side chain architecture at the phase transition.

ASSOCIATED CONTENT

Supporting Information. The following files are available free of charge. *Cryo*-EM Images: Estimation of backbone length. Dynamic light scattering data. Structural parameters from model fitting of the SANS data. Structural analysis of a P*b*E solution at 5 g L^{-1} in D_2O. Scattering contributions from different terms for the P*r*E solution (20 g L^{-1}) at 34 and 36 °C.

AUTHOR INFORMATION

Corresponding Author

*Christine M. Papadakis, papadakis@tum.de, phone +49 89 289 12 447, Fax +49 89 289 12 473 (C.M.P.).

Present Addresses

Author Contributions

The manuscript was written through contributions of all authors. All authors have given approval to the final version of the manuscript.

Funding Sources

This work benefited from the use of the SasView application, originally developed under NSF award DMR-0520547. SasView contains code developed with funding from the European Union's Horizon 2020 research and innovation programme under the SINE2020 project, grant agreement No 654000.

Notes

ACKNOWLEDGMENT

This work is based upon experiments performed at the KWS-1 instrument operated by JCNS at the Heinz Maier-Leibnitz Zentrum (MLZ), Garching, Germany. MLZ is acknowledged for beam time allocation and for providing excellent equipment.

References

1. Sheiko, S. S.; Sumerlin, B. S.; Matyjaszewski, K. Cylindrical Molecular Brushes: Synthesis, Characterization, and Properties. *Prog. Polym. Sci.* **2008**, *33*, 759-785.

2. Yuan, J.; Müller, A. H. E.; Matyjaszewski, K.; Sheiko, S. S., 6.06 - Molecular Brushes. In *Polymer Science: A Comprehensive Reference*, Matyjaszewski, K., Möller, M., Eds. Elsevier: Amsterdam, 2012; pp 199-264.

3. Verduzco, R.; Li, X.; Pesek, S. L.; Stein, G. E. Structure, Function, Self-Assembly, and Applications of Bottlebrush Copolymers. *Chem. Soc. Rev.* **2015**, *44*, 2405-2420.

4. Lee, H.-i.; Pietrasik, J.; Sheiko, S. S.; Matyjaszewski, K. Stimuli-Responsive Molecular Brushes. *Prog. Polym. Sci.* **2010**, *35*, 24-44.

5. Wu, C.; Wang, X. Globule-to-Coil Transition of a Single Homopolymer Chain in Solution. *Phys. Rev. Lett.* **1998**, *80*, 4092-4094.

6. Tavagnacco, L.; Zaccarelli, E.; Chiessi, E. On the Molecular Origin of the Cooperative Coil-to-Globule Transition of Poly(*N*-isopropylacrylamide) in Water. *Phys. Chem. Chem. Phys.* **2018**, *20*, 9997-10010.

7. Weber, C.; Rogers, S.; Vollrath, A.; Hoeppener, S.; Rudolph, T.; Fritz, N.; Hoogenboom, R.; Schubert, U. S. Aqueous Solution Behavior of Comb-Shaped Poly(2-ethyl-2-oxazoline). *J. Polym. Sci., Part A: Polym. Chem.* **2013**, *51*, 139-148.

8. Zhou, Y.; Tang, H.; Wu, P. Intra-Molecular Interactions Dominating the Dehydration of a Poly(2-isopropyl-2-oxazoline)-based Densely Grafted Polymer Comb in Aqueous Solution and Hysteretic Liquid–Liquid Phase Separation. *Phys. Chem. Chem. Phys.* **2017**, *19*, 6626-6635.

9. Rathgeber, S.; Pakula, T.; Wilk, A.; Matyjaszewski, K.; Beers, K. L. On the Shape of Bottle-Brush Macromolecules: Systematic Variation of Architectural Parameters. *J. Chem. Phys.* **2005**, *122*, 124904.

10. Hsu, H.-P.; Paul, W.; Rathgeber, S.; Binder, K. Characteristic Length Scales and Radial Monomer Density Profiles of Molecular Bottle-Brushes: Simulation and Experiment. *Macromolecules* **2010**, *43*, 1592-1601.

11. Pesek, S. L.; Li, X.; Hammouda, B.; Hong, K.; Verduzco, R. Small-Angle Neutron Scattering Analysis of Bottlebrush Polymers Prepared via Grafting-Through Polymerization. *Macromolecules* **2013**, *46*, 6998-7005.

12. Dalsin, S. J.; Hillmyer, M. A.; Bates, F. S. Molecular Weight Dependence of Zero-Shear Viscosity in Atactic Polypropylene Bottlebrush Polymers. *ACS Macro Lett.* **2014**, *3*, 423-427.

13. Pesek, S. L.; Xiang, Q.; Hammouda, B.; Verduzco, R. Small-Angle Neutron Scattering Analysis of Bottlebrush Backbone and Side Chain Flexibility. *J. Polym. Sci., Part B: Polym. Phys.* **2017**, *55*, 104-111.

14. Bejagam, K. K.; Singh, S. K.; Ahn, R.; Deshmukh, S. A. Unraveling the Conformations of Backbone and Side Chains in Thermosensitive Bottlebrush Polymers. *Macromolecules* **2019**, *52*, 9398-9408.

15. Li, C.; Gunari, N.; Fischer, K.; Janshoff, A.; Schmidt, M. New Perspectives for the Design of Molecular Actuators: Thermally Induced Collapse of Single Macromolecules from Cylindrical Brushes to Spheres. *Angew. Chem. Int. Ed.* **2004**, *43*, 1101-1104.

16. Li, X.; ShamsiJazeyi, H.; Pesek, S. L.; Agrawal, A.; Hammouda, B.; Verduzco, R. Thermoresponsive PNIPAAM Bottlebrush Polymers with Tailored Side-Chain Length and End-Group Structure. *Soft Matter* **2014**, *10*, 2008-2015.

17. Schulz, B.; Chudoba, R.; Heyda, J.; Dzubiella, J. Tuning the Critical Solution Temperature of Polymers by Copolymerization. *J. Chem. Phys.* **2015**, *143*, 243119.

18. Yamamoto, S.-i.; Pietrasik, J.; Matyjaszewski, K. ATRP Synthesis of Thermally Responsive Molecular Brushes from Oligo(ethylene oxide) Methacrylates. *Macromolecules* **2007**, *40*, 9348-9353.

19. Zhang, N.; Luxenhofer, R.; Jordan, R. Thermoresponsive Poly(2-Oxazoline) Molecular Brushes by Living Ionic Polymerization: Modulation of the Cloud Point by Random and Block Copolymer Pendant Chains. *Macromol. Chem. Phys.* **2012**, *213*, 1963-1969.

20. Wilfert, S.; Iturmendi, A.; Henke, H.; Brüggemann, O.; Teasdale, I. Thermoresponsive Polyphosphazene-Based Molecular Brushes by Living Cationic Polymerization. *Macromol. Symp.* **2014**, *337*, 116-123.

21. Zhao, J.; Mountrichas, G.; Zhang, G.; Pispas, S. Thermoresponsive Core−Shell Brush Copolymers with Poly(propylene oxide)-*block*-poly(ethylene oxide) Side Chains via a “Grafting From” Technique. *Macromolecules* **2010**, *43*, 1771-1777.

22. Zhao, J.; Zhang, G.; Pispas, S. Thermoresponsive Brush Copolymers with Poly(propylene oxide-*ran*-ethylene oxide) Side Chains via Metal-Free Anionic Polymerization “Grafting From” Technique. *J. Polym. Sci., Part A: Polym. Chem.* **2010**, *48*, 2320-2328.

23. Armstrong, J.; Chowdhry, B.; O'Brien, R.; Beezer, A.; Mitchell, J.; Leharne, S. Scanning Microcalorimetric Investigations of Phase Transitions in Dilute Aqueous Solutions of Poly(oxypropylene). *J. Phys. Chem.* **1995**, *99*, 4590-4598.

24. Saeki, S.; Kuwahara, N.; Nakata, M.; Kaneko, M. Upper and Lower Critical Solution Ttemperatures in Poly(ethylene glycol) solutions. *Polymer* **1976**, *17*, 685-689.

25. Saraiva, A.; Persson, O.; Fredenslund, A. An Experimental Investigation of Cloud-Point Curves for the Poly(ethylene glycol)/Water System at Varying Molecular Weight Distributions. *Fluid Ph. Equilibria* **1993**, *91*, 291-311.

26. Batrakova, E. V.; Kabanov, A. V. Pluronic Block Copolymers: Evolution of Drug Delivery Concept from Inert Nanocarriers to Biological Response Modifiers. *J. Control. Release* **2008**, *130*, 98-106.

27. Pitto-Barry, A.; Barry, N. P. E. Pluronic® Block-Copolymers in Medicine: From Chemical and Biological Versatility to Rationalisation and Clinical Advances. *Polym. Chem.* **2014**, *5*, 3291-3297.

28. Schulz, A.; Jaksch, S.; Schubel, R.; Wegener, E.; Di, Z.; Han, Y.; Meister, A.; Kressler, J.; Kabanov, A. V.; Luxenhofer, R.; Papadakis, C. M.; Jordan, R. Drug-Induced Morphology Switch in Drug Delivery Systems Based on Poly(2-oxazoline)s. *ACS Nano* **2014**, *8*, 2686-2696.

29. Jaksch, S.; Schulz, A.; Di, Z.; Luxenhofer, R.; Jordan, R.; Papadakis, C. M. Amphiphilic Triblock Copolymers from Poly(2-oxazoline) with Different Hydrophobic Blocks: Changes of the Micellar Structures upon Addition of a Strongly Hydrophobic Cancer Drug. *Macromol. Chem. Phys.* **2016**, *217*, 1448-1456.

30. Kripotou, S.; Psylla, C.; Kyriakos, K.; Raftopoulos, K. N.; Zhao, J.; Zhang, G.; Pispas, S.; Papadakis, C. M.; Kyritsis, A. Structure and Crystallization Behavior of Poly(ethylene oxide) (PEO) Chains in Core–Shell Brush Copolymers with Poly(propylene oxide)-*block*-poly(ethylene oxide) Side Chains. *Macromolecules* **2016**, *49*, 5963-5977.

31. Streitwieser, A.; Heathcock, C. H.; Kosower, E. M.; Corfield, P. J., *Introduction to Organic Chemistry*. Macmillan New York: 1992.

32. Kimanius, D.; Forsberg, B. O.; Scheres, S. H. W.; Lindahl, E. Accelerated *Cryo*-EM Structure Determination with Parallelisation Using GPUs in RELION-2. *eLife* **2016**, *5*, e18722.

33. Zivanov, J.; Nakane, T.; Forsberg, B. O.; Kimanius, D.; Hagen, W. J. H.; Lindahl, E.; Scheres, S. H. W. New Tools for Automated High-Resolution *Cryo*-EM Structure Determination in RELION-3. *eLife* **2018**, *7*, e42166.

34. Zheng, S. Q.; Palovcak, E.; Armache, J.-P.; Verba, K. A.; Cheng, Y.; Agard, D. A. MotionCor2: Anisotropic Correction of Beam-Induced Motion for Improved *Cryo*-Electron Microscopy. *Nat. Methods* **2017**, *14*, 331-332.

35. Schindelin, J.; Arganda-Carreras, I.; Frise, E.; Kaynig, V.; Longair, M.; Pietzsch, T.; Preibisch, S.; Rueden, C.; Saalfeld, S.; Schmid, B.; Tinevez, J.-Y.; White, D. J.; Hartenstein, V.; Eliceiri, K.; Tomancak, P.; Cardona, A. Fiji: an Open-Source Platform for Biological-Image Analysis. *Nat. Methods* **2012**, *9*, 676-682.

36. Štěpánek, P., Data Analysis in Dynamic Light Scattering. In *Dynamic Light Scattering: The Method and Some Applications (Monographs on the Physics and Chemistry of Materials)*, Brown, W., Ed. Clarendon Press: New York, 1993; pp 177–241.

37. Jakeš, J. Regularized Positive Exponential Sum (REPES) Program - A Way of Inverting Laplace Transform Data Obtained by Dynamic Light Scattering. *Collect. Czech. Chem. Commun.* **1995**, *60*, 1781–1797.

38. Heinz Maier-Leibnitz Zentrum; et al. KWS-1: Small-Angle Scattering Diffractometer. *Journal of large-scale research facilities* **2015**, *1*, A28.

39. Feoktystov, A. V.; Frielinghaus, H.; Di, Z.; Jaksch, S.; Pipich, V.; Appavou, M.-S.; Babcock, E.; Hanslik, R.; Engels, R.; Kemmerling, G.; Kleines, H.; Ioffe, A.; Richter, D.; Bruckel, T. KWS-1 High-Resolution Small-Angle Neutron Scattering Instrument at JCNS: Current State. *J. Appl. Crystallogr.* **2015**, *48*, 61-70.

40. Kotlarchyk, M.; Chen, S. H. Analysis of Small Angle Neutron Scattering Spectra from Polydisperse Interacting Colloids. *J. Chem. Phys.* **1983**, *79*, 2461-2469.

41. Berr, S. S. Solvent Isotope Effects on Alkytrimethylammonium Bromide Micelles as a Function of Alkyl Chain Length. *J. Phys. Chem.* **1987**, *91*, 4760-4765.

42. Nelson, A.; Cosgrove, T. Small-Angle Neutron Scattering Study of Adsorbed Pluronic Tri-Block Copolymers on Laponite. *Langmuir* **2005**, *21*, 9176-9182.

43. Percus, J. K.; Yevick, G. J. Analysis of Classical Statistical Mechanics by Means of Collective Coordinates. *Phys. Rev.* **1958**, *110*, 1-13.

44. Hammouda, B. A New Guinier-Porod Model. *J. Appl. Crystallogr.* **2010**, *43*, 716-719.

45. Koberstein, J. T.; Morra, B.; Stein, R. S. The Determination of Diffuse-Boundary Thicknesses of Polymers by Small-Angle X-ray Scattering. *J. Appl. Crystallogr.* **1980**, *13*, 34-45.

46. Schmidt, P. W. Interpretation of Small-Angle Scattering Curves Proportional to a Negative Power of the Scattering Vector. *J. Appl. Crystallogr.* **1982**, *15*, 567-569.

47. Stieger, M.; Pedersen, J. S.; Lindner, P.; Richtering, W. Are Thermoresponsive Microgels Model Systems for Concentrated Colloidal Suspensions? A Rheology and Small-Angle Neutron Scattering Study. *Langmuir* **2004**, *20*, 7283-7292.

48. Hammouda, B.; Ho, D. L.; Kline, S. Insight into Clustering in Poly(ethylene oxide) Solutions. *Macromolecules* **2004**, *37*, 6932-6937.

49. Hammouda, B.; Ho, D. L. Insight into Chain Dimensions in PEO/Water Solutions. *J. Polym. Sci., Part B: Polym. Phys.* **2007**, *45*, 2196-2200.

50. http://www.sasview.org/ (accessed Septemper 30, 2019).

51. Foster, B.; Cosgrove, T.; Hammouda, B. Pluronic Triblock Copolymer Systems and Their Interactions with Ibuprofen. *Langmuir* **2009**, *25*, 6760-6766.

52. Israelachvili, J. N.; Mitchell, D. J.; Ninham, B. W. Theory of Self-Assembly of Hydrocarbon Amphiphiles into Micelles and Bilayers. *J. Chem. Soc. Faraday Trans. 2* **1976**, *72*, 1525-1568.

53. Ganguly, R.; Choudhury, N.; Aswal, V. K.; Hassan, P. A. Pluronic L64 Micelles near Cloud Point: Investigating the Role of Micellar Growth and Interaction in Critical Concentration Fluctuation and Percolation. *J. Phys. Chem. B* **2009**, *113*, 668-675.

54. Filippov, A.; Tarabukina, E.; Kudryavtseva, A.; Fatullaev, E.; Kurlykin, M.; Tenkovtsev, A. Molecular Brushes with Poly-2-ethyl-2-oxazoline Side Chains and Aromatic Polyester Backbone Manifesting Double Stimuli Responsiveness. *Colloid Polym. Sci.* **2019**, *297*, 1445-1454.

55. Tanaka, H. Appearance of a Moving Droplet Phase and Unusual Networklike or Spongelike Patterns in a Phase-Separating Polymer Solution with a Double-well-shaped Phase Diagram. *Macromolecules* **1992**, *25*, 6377-6380.

56. Tanaka, H. Viscoelastic Phase Separation. *J. Phys. Condens. Matter* **2000**, *12*, R207-R264.

57. Niebuur, B.-J.; Claude, K.-L.; Pinzek, S.; Cariker, C.; Raftopoulos, K. N.; Pipich, V.; Appavou, M.-S.; Schulte, A.; Papadakis, C. M. Pressure-Dependence of Poly(*N*-isopropylacrylamide) Mesoglobule Formation in Aqueous Solution. *ACS Macro Lett.* **2017**, *6*, 1180-1185.